Pressure dependence on the remanent magnetization of Fe-Ni alloys and Ni metal

Qingguo Wei,* Stuart Alan Gilder,† and Bernd Maier‡
Department of Earth and Environmental Sciences, Ludwig Maximilians Universität, 80333 Munich, Germany
(Received 14 July 2014; revised manuscript received 24 September 2014; published 21 October 2014)

We measured the acquisition of magnetic remanence of iron-nickel alloys ($Fe_{64}Ni_{36}$, $Fe_{58}Ni_{42}$, and $Fe_{50}Ni_{50}$) and pure Ni under pressures up to 23 GPa at room temperature. Magnetization decreases markedly for $Fe_{64}Ni_{36}$ between 5 and 7 GPa yet remains ferromagnetic until at least 16 GPa. Magnetization rises by a factor of 2–3 for the other compositions during compression to the highest applied pressures. Immediately upon decompression, magnetic remanence increases for all Fe-Ni alloys while magnetic coercivity remains fairly constant at relatively low values (5–20 mT). The amount of magnetization gained upon complete decompression correlates with the maximum pressure experienced by the sample. Martensitic effects best explain the increase in remanence rather than grain-size reduction, as the creation of single domain sized grains would raise the coercivity. The magnetic remanence of low Ni Invar alloys increases faster with pressure than for other body-centered-cubic compositions due to the higher magnetostriction of the low Ni Invar metals. Thermal demagnetization spectra of $Fe_{64}Ni_{36}$ measured after pressure release broaden as a function of peak pressure, with a systematic decrease in Curie temperature. Irreversible strain accumulation from the martensitic transition likely explains the broadening of the Curie temperature spectra, consistent with our x-ray diffraction analyses.

DOI: 10.1103/PhysRevB.90.144425 PACS number(s): 91.60.Gf, 75.50.Bb, 91.60.Pn, 75.60.Ej

I. INTRODUCTION

After iron, metallic nickel comprises the second major constituent in the cores of terrestrial planets, as well as Earth's moon and Jupiter's moon Ganymede [1–3]. Nickel concentrations vary from 5% to 60% in iron meteorites, which once formed the cores of differentiated protoplanets [4,5]. As summarized by Reuter *et al.* [6] and Goldstein *et al.* [5] the phase diagram of Fe-Ni alloys at Earth-like ambient conditions depends largely on the cooling rate and the concentration of lighter elements (P, C, etc.). Iron-nickel metals with Ni concentrations lower than ∼12% by weight have a body-centered-cubic (bcc) structure while those above 51% Ni have face-centered-cubic (fcc) structures. Phases in between 5%–12% Ni and 51% Ni are metastable; they form in a miscibility gap with mixed bcc and fcc phases, although single bcc or fcc phases can be stabilized in the gap region when rapidly quenched. Compositions around $Fe_{64}Ni_{36}$ (fcc), called Invar, exhibit near-null thermal expansion, making them useful for technological applications.

The magnetic moments of the Fe-Ni alloys systematically decrease from ∼2.2 Bohr magnetons for pure Fe to ∼0.6 in pure Ni, with a deflection at the Invar compositions [7,8]. Magnetic susceptibility mimics this trend [Fig. 1(a)]. Curie temperatures of the bcc phases decrease from 770 °C for pure Fe to 740 °C for ∼$Fe_{92}Ni_{10}$, then drop steeply above ∼10% Ni [Fig. 1(b)]. Curie temperatures of the fcc phases are below room temperature for Invar compositions with <30% Ni, then increase until attaining a maximum of ∼570 °C at $Fe_{30}Ni_{70}$, and then drop to ∼370 °C at Ni_{100} [Fig. 1(b)] [9,10]. Magnetocrystalline anisotropy and magnetostriction attain maxima at around 40% Ni in the fcc alloys [11].

Models explaining the Invar effect evoke magnetovolume effects (volume dependence on exchange interaction) that compensate for thermal expansion [12–14]. Such models bear on the magnetic behavior of Invar under pressure, as evinced by several experiments—most notably on the Curie temperature. Indeed, changes in Curie temperature with pressure goes from sharply negative at the low Ni Invar compositions (−35 K/GPa for $Fe_{64}Ni_{36}$) to negative yet with lower slopes as Ni increases (−29 and −21 K/GPa for $Fe_{58}Ni_{42}$ and $Fe_{50}Ni_{50}$); the slope becomes positive for fcc compositions above ∼65% Ni and is 4 K/GPa for Ni_{100} [13,15–17]. Mössbauer spectroscopy measured at 4.2 K on $Fe_{68.5}Ni_{31.5}$ and $Fe_{65}Ni_{35}$ show that hyperfine field distributions break down under pressure until collapsing by 5.8 and 7 GPa, respectively [18]. X-ray emission spectroscopy of $Fe_{64}Ni_{36}$ under pressure at ambient temperature reveals that the amplitude of the Fe local magnetic moment changes in a two-step manner—once at 5 GPa and again at 15 GPa, above which any trace of ferromagnetic character was lost [19]. Orbital magnetic moments measured with x-ray magnetic circular dichroism (XMCD) under pressure on $Fe_{64}Ni_{36}$ decrease by 50% around 3–4 GPa, then remain at that level until 10 GPa [20]. Using the extended x-ray absorption fine structure technique on $Fe_{65}Ni_{35}$, Matsumoto *et al.* [21] found that the magnetic dichroic amplitude is highly suppressed by 6 GPa and disappears around 7 GPa. Matsumoto *et al.* [21] ascribed the discrepancy with the results of Nataf *et al.* [20] due to the martensitic nature of the transition.

In this paper, we document magnetic remanence measurements made under compression and decompression on $Fe_{64}Ni_{36}$, $Fe_{58}Ni_{42}$, $Fe_{50}Ni_{50}$, and Ni_{100} powders up to maximum pressures of 23.0 GPa. Because magnetovolume effects are greatest at Invar compositions around $Fe_{64}Ni_{36}$, we anticipated finding magnetic remanence near that composition to be more pressure sensitive than the rest. We also sought to confirm the negative slope in the Curie temperature by testing whether magnetization was lost at prescribed pressures. For example, $Fe_{64}Ni_{36}$ has a Curie temperature of 208 °C at

*wei@geophysik.uni-muenchen.de
†gilder@lmu.de
‡bernd.maier@lmu.de

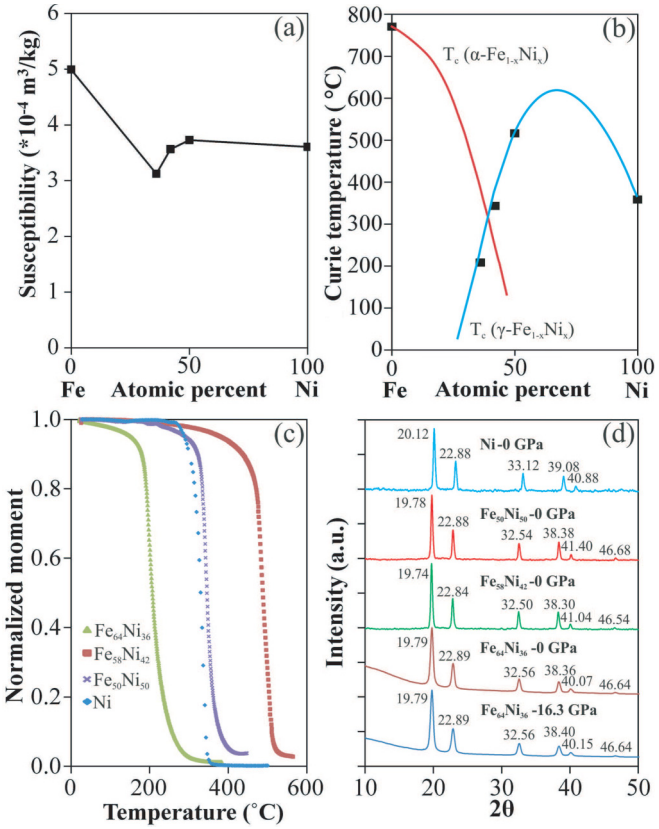

FIG. 1. (Color online) Magnetic and physical properties of the iron-nickel alloys used in this study. (a) Magnetic susceptibility. (b) Curie temperature trends for bcc, α-$Fe_{1-x}Ni_x$ (red curve; Chuang *et al.* [22]) and fcc, γ-$Fe_{1-x}Ni_x$ (blue curve; Crangle and Hallam [7]). Black squares represent the data from our samples derived from the second derivative of the curves in Fig. 1(c). (c) Magnetization normalized to the initial (room temperature) value versus temperature for the four Fe-Ni metals used in this study. (d) X-ray powder diffraction patterns demonstrating a pure fcc phase for all compositions. The top three patterns were measured with a STOE STADI P diffractometer using Mo-$K\alpha_1$ radiation ($\lambda = 0.709$ Å); bottom two were measured with an Agilent Gemini diffractometer using Mo-$K\alpha$ radiation ($\lambda = 0.7107$ Å). Bottommost spectrum was obtained upon pressure release (ambient conditions) from 16.3 GPa.

ambient pressure. Given that its Curie temperature decreases by 35 K/GPa, one would predict a complete loss in magnetization at about 5.2 GPa at room temperature.

II. EXPERIMENTAL PROCEDURE AND RESULTS

Our experiments used polycrystalline samples of $Fe_{64}Ni_{36}$, $Fe_{58}Ni_{42}$, $Fe_{50}Ni_{50}$, and Ni_{100} (Goodfellow, purity >99.5%, max particle size 45 μm). Magnetic hysteresis loops measured on all samples with a Petersen Instruments, variable field translation balance at ambient conditions yield remanence ratios [remanent magnetization after saturation (Mrs)/saturation magnetization (Ms)] <0.1 and coercivity ratios [coercivity of remanence (Bcr)/bulk coercivity (Bc)] > 7, characteristic of multidomain material. Curie temperatures measured with the same balance in a 30 mT field, and defined by the second derivative of the data, are 208 °C, 343 °C, 516 °C, and 358 °C for $Fe_{64}Ni_{36}$, $Fe_{58}Ni_{42}$, $Fe_{50}Ni_{50}$, and Ni_{100}, respectively [Fig. 1(c)]. The decrease in magnetization occurs over several tens of degrees for $Fe_{64}Ni_{36}$ and $Fe_{58}Ni_{42}$ [Fig. 1(c)], which could indicate nonstoichiometry, yet their Curie temperatures are consistent with published values at the average compositions [Fig. 1(b)] [7,10,22,23]. The other phases show sharper drops in moment with increasing temperature near the Curie temperature. Magnetic susceptibility (Bartington MS2) of the samples diluted in silica gel (~15% wt % metal) decrease linearly from pure Fe (50×10^{-5} m^3/kg) to pure Ni (31×10^{-5} m^3/kg) with a deflection at $Fe_{64}Ni_{36}$ [Fig. 1(a)], following the trend in magnetic moment of the Fe-Ni alloys [23,24]. Powder x-ray diffraction using an x-ray source wavelength of 0.709 Å (Mo $K\alpha_1$) identifies solely fcc structures in all samples with no evidence for bcc or oxide phases [Fig. 1(d)].

In each experiment, polycrystalline material was loaded together with ruby spheres and silica gel into a cylindrical chamber drilled in a work-hardened gasket that was contained within a pressure cell consisting of Be-Cu metal and moissanite anvils. Three independent experiments were made for $Fe_{64}Ni_{36}$—two of them using 700-μm-diameter culets with beryllium-copper gaskets (chamber size = diameter 390 μm, height 250 μm) and the third using 400-μm-diameter culets with a rhenium gasket whose initial chamber dimensions were diameter 250 μm and height 175 μm. Experiments on $Fe_{58}Ni_{42}$, $Fe_{50}Ni_{50}$ and two on Ni_{100} (Ni-1 and Ni-2) used 400 μm culet diameter moissanite anvils with rhenium gaskets containing cylindrical chambers of diameter 200 μm and height 160–180 μm. Although less hydrostatic than some pressure media (methanol, etc.), silica gel is preferable because the sample can be loaded into the cell while insuring none rests outside the chamber. Pressure was measured before and after each experiment using ruby fluorescence spectroscopy with a Coherent, Cube 405-nm laser and a Princeton Instruments (PIXIS) charged coupled device connected to a 150-mm, ARC SpectraPro spectrometer. Rubies placed near the center and edge of the sample chamber helped monitor potential pressure gradients. Discussion below reports the average, not peak, pressures—both are listed in Table I.

For each experiment at successive pressure steps, we measured the stepwise acquisition of isothermal remanent magnetization (Fig. 2). A static field was directed perpendicular to the axis of the moissanite pistons with an electromagnet whose pole pieces slide through the cell's housing until they abut the pistons. First we applied a magnetic field of 370 mT along the $-y$-axis direction, which produces a magnetization with a declination of 270° and an inclination of 0° since magnetization along the x and z axes are negligible. The cell was removed from the electromagnet and then placed into the bore of a 2G Enterprises Inc., three-axis, superconducting magnetometer to measure the full magnetic vector. This first data point is considered as a starting point (0 mT). We then stepwise increased the applied field intensity in the $+y$-axis direction until reaching 370 mT, each time measuring the corresponding remanence with the magnetometer. Initially the magnetization is reduced with no change in direction. At higher applied fields approaching the coercivity of the sample, the moment along the y axis becomes negligible and the declination moves out of parallel with the y axis. Upon

TABLE I. Data for iron-nickel alloys and pure nickel from this study. P_{ave}, average pressure; P_{max}, maximum pressure; SIRM, saturation isothermal remanent magnetization; Bcr, coercivity of remanence; S_{corr}, correction made to the SIRM data to account for the change in demagnetizing factor due to the increasing degree of oblateness. $SIRM_{norm}$ is the SIRM normalized by the initial value after accounting for S_{corr}, e.g., $(SIRM_{p=n}/S_{corr})/(SIRM_{p=i}/S_{corr})$. h/d, height to average diameter ratio of sample chamber.

P_{ave} (GPa)	P_{max} (GPa)	SIRM ($\times 10^9$ Am^2)	Bcr (mT)	S_{corr} ($\times 10^{-3}$)	$SIRM_{norm}$	h/d
			$Fe_{64}Ni_{36}$-1			
0.0	0.0	11.6	13.4	1.17	1.0	0.6
1.5	1.5	14.3	11.5	1.17	1.2	0.6
2.3	2.6	18.2	10.3	1.17	1.6	0.6
3.3	3.7	22.7	9.1	1.17	2.0	0.6
4.6	5.2	32.5	7.8	1.24	2.7	0.6
5.3	6.3	33.4	7.6	1.30	2.6	0.5
6.6	8.1	29.3	7.7	1.67	1.8	0.4
7.5	9.4	25.1	7.7	1.74	1.5	0.3
4.6	5.7	52.3	7.7	1.74	3.0	0.3
2.0	2.6	66.6	8.0	1.74	3.9	0.3
0.0	0.0	74.3	8.4	1.74	4.3	0.3
			$Fe_{64}Ni_{36}$-2			
0.0	0.0	10.4	11.8	1.11	1.0	0.7
2.5	2.8	21.4	9.3	1.27	1.8	0.5
4.8	5.9	32.9	6.9	1.70	2.1	0.3
7.2	9.2	19.2	6.4	1.70	1.1	0.3
			$Fe_{64}Ni_{36}$-3			
0.2	0.2	7.0	19.6	1.07	1.0	0.7
2.5	2.6	9.7	12.2	1.14	1.3	0.6
4.8	5.0	15.8	8.3	1.33	1.8	0.5
7.2	7.4	9.3	9.1	1.33	1.1	0.5
8.7	9.0	7.3	10.1	1.33	0.8	0.5
10.0	10.5	6.4	10.3	1.35	0.7	0.5
11.8	12.7	6.1	10.3	1.35	0.7	0.5
13.8	15.0	6.6	10.2	1.35	0.8	0.5
15.2	16.8	7.6	10.2	1.35	0.9	0.5
16.3	18.7	7.7	9.9	1.35	0.9	0.5
12.8	15.4	11.1	8.5	1.35	1.3	0.5
10.7	12.3	18.1	8.1	1.35	2.1	0.5
7.2	9.0	35.3	8.1	1.35	4.0	0.5
5.9	7.2	51.4	7.8	1.35	5.9	0.5
3.8	4.6	72.6	7.4	1.35	8.3	0.5
0.0	0.0	83.5	7.5	1.35	9.5	0.5
			$Fe_{58}Ni_{42}$			
0.3	0.3	11.3	12.3	1.00	1.0	0.8
2.5	2.6	19.2	12.7	1.00	1.7	0.8
4.3	4.6	21.8	12.3	1.25	1.5	0.5
6.5	6.7	25.0	9.6	1.27	1.7	0.5
8.5	9.1	24.9	9.0	1.31	1.7	0.5
10.4	10.6	29.0	8.2	1.35	1.9	0.5
12.3	12.7	28.3	8.2	1.39	1.8	0.5
15.0	15.8	25.3	8.3	1.57	1.4	0.4
18.5	20.4	25.7	8.3	1.57	1.4	0.4
20.3	22.7	26.4	8.6	1.57	1.5	0.4
17.3	19.6	37.2	7.8	1.57	2.1	0.4
14.6	17.1	45.2	8.2	1.57	2.5	0.4
10.2	12.2	59.1	8.1	1.57	3.3	0.4
8.0	9.5	62.9	8.5	1.57	3.5	0.4
4.8	5.6	73.5	8.9	1.57	4.1	0.4
0.3	0.3	86.9	9.2	1.57	4.9	0.4
			$Fe_{50}Ni_{50}$			
0.1	0.1	8.1	26.9	0.93	1.0	0.9
2.8	2.9	10.8	24.4	0.95	1.3	0.8
5.0	5.2	12.1	21.4	0.97	1.4	0.8
7.5	7.6	14.0	17.3	0.99	1.6	0.8
9.2	9.3	15.8	13.7	1.03	1.8	0.7
11.3	11.4	17.5	11.8	1.06	1.9	0.7
13.3	13.5	18.5	11.4	1.09	1.9	0.7
16.0	16.5	19.5	9.1	1.12	2.0	0.6
18.9	19.6	19.5	7.1	1.12	2.0	0.6
21.3	22.2	22.1	6.5	1.12	2.3	0.6
23.0	24.0	23.8	5.3	1.12	2.4	0.6
21.2	22.7	24.7	6.0	1.12	2.5	0.6
19.8	21.2	25.2	6.6	1.12	2.6	0.6
16.9	17.9	29.0	6.5	1.12	3.0	0.6
11.1	12.3	33.5	7.4	1.12	3.4	0.6
10.2	11.4	37.8	7.8	1.12	3.9	0.6
8.4	9.3	39.0	7.9	1.12	4.0	0.6
5.2	6.1	45.5	7.6	1.12	4.7	0.6
0.4	0.4	45.1	8.1	1.12	4.6	0.6
			Ni-1			
0.2	0.2	20.0	13.3	0.91	1.0	0.9
2.9	3.1	27.1	18.2	0.91	1.4	0.9
7.1	7.5	33.4	19.1	1.14	1.3	0.6
10.0	10.6	41.3	20.3	1.31	1.4	0.5
11.0	13.2	42.9	18.8	1.35	1.5	0.5
5.9	6.6	59.3	12.0	1.02	2.7	0.7
4.1	4.6	70.4	11.8	1.02	3.2	0.7
0.0	0.0	122.0	9.4	1.02	5.5	0.7
			Ni-2			
0.2	0.2	9.8	26.3	0.9	1.0	0.8
4.0	4.1	13.0	30.2	0.9	1.3	0.8
6.2	6.2	14.3	30.0	1.0	1.4	0.8
9.3	9.6	18.5	31.4	1.1	1.7	0.7
10.3	10.7	21.7	26.4	1.3	1.7	0.5
11.8	12.5	23.8	25.6	1.4	1.6	0.4
13.4	14.5	25.7	23.8	1.7	1.5	0.3
15.2	16.9	29.9	23.7	1.7	1.6	0.3
17.2	19.6	33.5	23.3	1.9	1.7	0.3
15.3	17.7	37.1	21.4	1.9	1.8	0.3
13.2	15.6	42.0	21.0	1.9	2.1	0.3
15.8	18.0	38.0	22.4	1.9	1.9	0.3
17.2	19.7	39.8	22.5	2.0	1.9	0.3
15.1	17.9	47.3	20.4	2.0	2.3	0.3
12.6	15.3	50.2	18.8	2.0	2.4	0.3
9.7	12.0	53.6	17.8	2.0	2.5	0.3
6.6	8.3	53.8	17.9	2.0	2.5	0.3
4.2	4.8	63.0	18.4	2.0	3.0	0.3
0.1	0.1	158.3	14.1	2.0	7.4	0.3

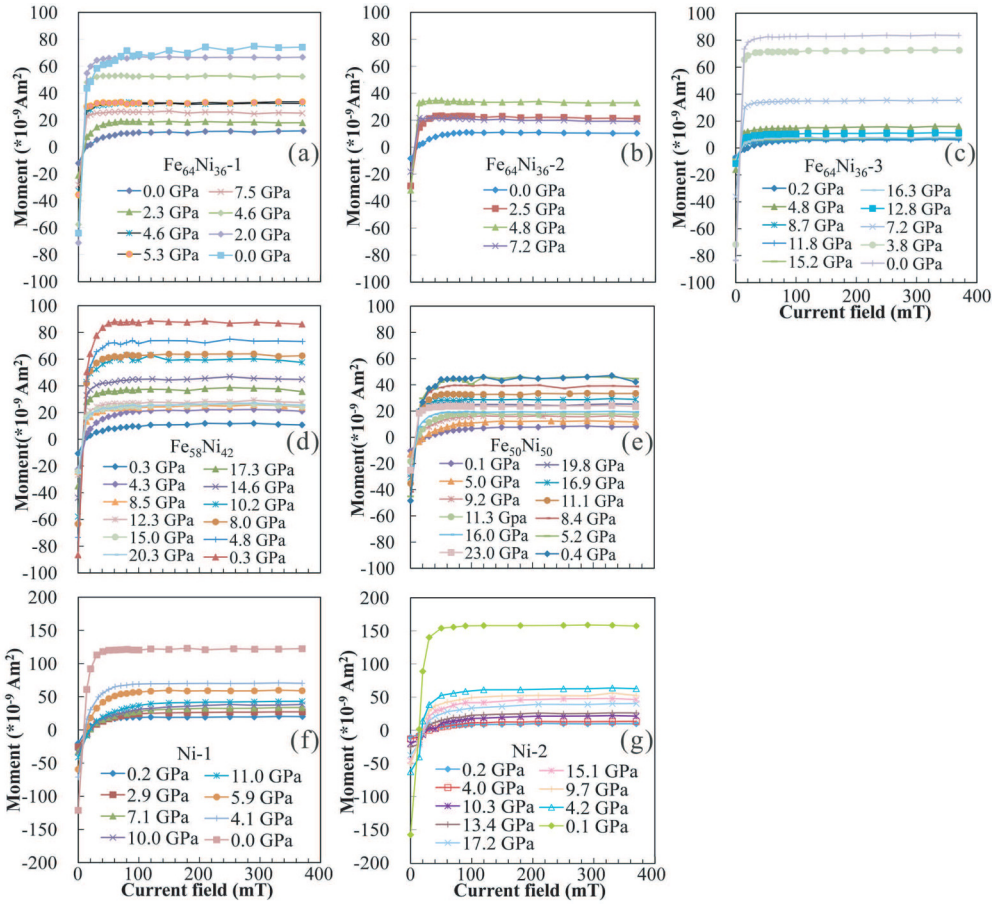

FIG. 2. (Color online) (a)–(c) Backfield magnetization acquisition curves for three independent experiments on $Fe_{64}Ni_{36}$ powder. (d), (e) Backfield magnetization curves for $Fe_{58}Ni_{42}$ and $Fe_{50}Ni_{50}$. (f), (g) Backfield magnetization acquisition curves for independent experiments on Ni_{100} powder. Some pressure steps are omitted to better distinguish the curves; all pressure steps are given in Table I.

stronger applied fields, the y-axis moment strengthens and declination converges to 90° (inclination is still ~0°). At the end of the experiment, the absolute magnetic moment should equal the moment at the start.

The same type of experiment is made before loading the sample into the gasket in order to measure the contribution from the empty cell. These data are subtracted from the backfield curves measured with the loaded cell (Fig. 2). Once completed, the pressure is raised or lowered and then the process is repeated on the same sample. Two magnetic parameters can be extracted from the backfield curves: The coercivity of remanence (Bcr), defined as the magnetic field in mT required to null the remanent magnetization, and the saturation isothermal remanent magnetization (SIRM, in units of Am^2), which is defined here as the average moment (y axis only) from the last three steps of the backfield curves. This definition assumes the sample becomes fully saturated by the last three steps, consistent with the data. The goal is to see how Bcr and SIRM change as a function of pressure.

In the first experiment on $Fe_{64}Ni_{36}$, pressure was progressively raised to 7.5 GPa and then progressively decompressed to ambient conditions. In the second experiment, we again progressively compressed to 7.2 GPa, whereafter the pressure was lost and the experiment was aborted (no decompression path). In the third experiment, we stepwise compressed the sample to 16.3 GPa and then stepwise decompressed to ambient conditions. $Fe_{58}Ni_{42}$ and $Fe_{50}Ni_{50}$ were progressively compressed to 20.3 and 23.0 GPa, respectively, and then progressively decompressed back to ambient conditions. For Ni_{100}, the two experiments reached maximum pressures of 11.0 and 17.2 GPa (Ni-1 and Ni-2) that were progressively decompressed to ambient conditions. A secondary pressure cycle between 17.2 and 13.2 GPa was made for Ni-2.

Figure 3 plots the relative change in SIRM ($SIRM_{norm}$ in Table I) and the absolute change in Bcr as a function of pressure at room temperature. Magnetization is mass dependent whereas coercivity is not. Because the samples' masses are unknown in our experiments, relative values are used for SIRM in order to compare the results. The SIRM data require a shape correction because sample geometry influences magnetization intensity depending on the degree of oblateness and the direction of the applied field relative to the plane of the oblate spheroid [25]. For this reason we measured the horizontal cell dimensions (front and back sides) at each pressure step with a Leica MZ12.5 microscope fitted with a DSC295 digital camera (1 μm resolution) (Table I).

The initial height to diameter ratio (h/d) of the sample chambers ranged from 0.5 to 0.9. Those <0.8 already deviate from spherical isotropy. Higher pressures decrease h/d, resulting in higher degrees of oblateness and lower demagnetization

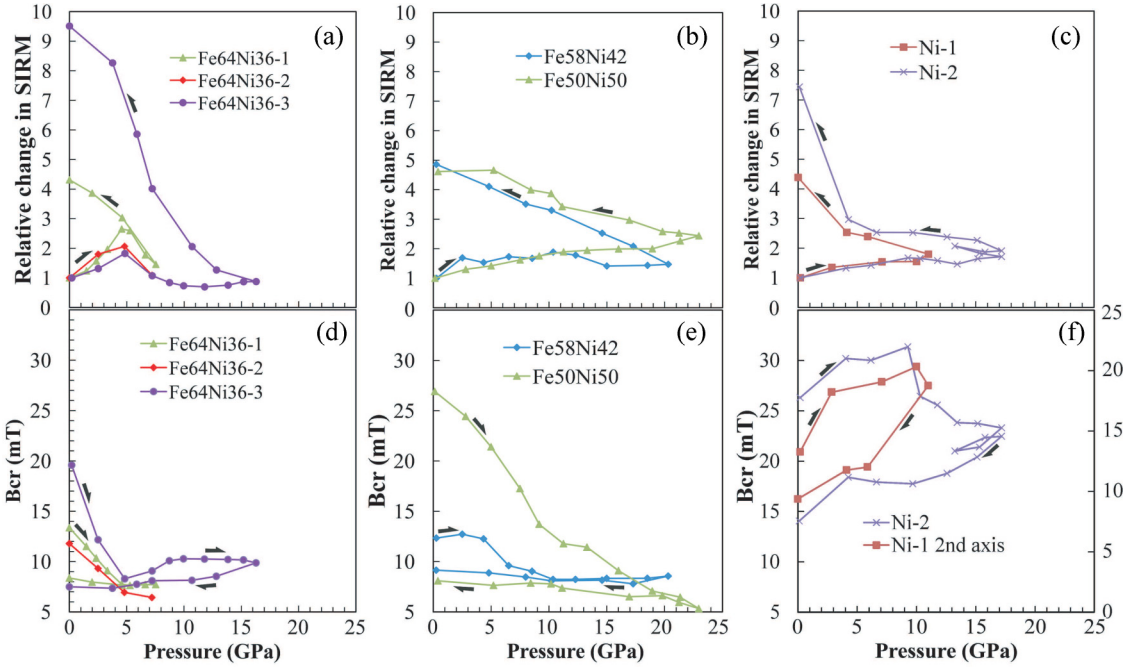

FIG. 3. (Color online) (a)–(c) Normalized SIRM and (d)–(f) coercivity of remanence (Bcr) as a function of pressure for $Fe_{64}Ni_{36}$, $Fe_{58}Ni_{42}$, $Fe_{50}Ni_{50}$, and Ni_{100}. SIRM was normalized after shape correction. Arrows indicate the pressure path; data from Table I.

factors in the long axis (d) direction; e.g., the direction perpendicular to the maximum compression axis. Because the applied field direction lies along the long axis of the sample, increasing the maximum to minimum axis ratio will have the apparent effect of decreasing Bcr while increasing SIRM [26]. We can correct for the change in demagnetization factor by normalizing the SIRM values for the change in shape (S_{corr}) via a power function $S_{corr} = 8.36 \times 10^{-4}(h/d)^{-0.66}$ [25]. In other words, if h/d is flattened from 0.8 to 0.3, SIRM will increase 1.9 times and Bcr will decrease ~20% in the long axis plane. Sample geometry changes insignificantly during decompression with respect to that obtained at the highest pressure, so changes in magnetization observed along the decompression path can be directly compared with respect to the highest pressure step. The shape contribution was accounted for in all SIRM data in Fig. 3. Those data are used in the subsequent discussion.

The three experiments on $Fe_{64}Ni_{36}$ show a high degree of reproducibility with a two- to threefold increase in SIRM by 5 GPa, whereafter SIRM decreases to near-initial (precompression) values by 6–7 GPa. That SIRM decreases above ~5 GPa should be expected based on prior work suggesting the Curie temperature decreases by 35 K/GPa. Experiment No. 3 that goes to the highest pressure contains our most unexpected observations as the magnetization significantly increases immediately upon decompression—by 10.7 GPa, the magnetization is already two times greater than the initial value. In all experiments with $Fe_{64}Ni_{36}$, Bcr decreases until 5 GPa whereafter it remains fairly constant, including upon decompression. The applied magnetic field increments are 15,20,30,40, . . . mT; we cannot achieve fields lower than 15 mT due to an intrinsic, permanent remanence of the electromagnet. Uncertainties on the Bcr data depend on the magnetization intensity crossing the y axis going from negative to positive values.

SIRM of $Fe_{58}Ni_{42}$ increases twofold until ~11 GPa, whereafter it slightly decreases upon further compression. SIRM moments of $Fe_{50}Ni_{50}$ and Ni_{100} increase fairly continuously with pressure during compression; all phases exhibit significant increases in magnetization upon decompression. Magnetization for $Fe_{58}Ni_{42}$ and $Fe_{50}Ni_{50}$ increases fairly linearly upon decompression, becoming 4–5 times stronger than initially. In contrast, SIRM of Ni increases abruptly at the last decompression step. Typical of most magnetic phases, the amount of increase upon full decompression relative to starting depends on the maximum pressure. Bcr for $Fe_{58}Ni_{42}$ and $Fe_{50}Ni_{50}$ decreases with increasing pressure until plateauing; it stays low and fairly constant upon decompression. Bcr for Ni_{100} increases until 10 GPa, followed by a continuous decrease. For the Invar compositions, up to 20% of the initial decrease in Bcr can be attributed to changes in shape, which is not accounted for in Fig. 3.

III. DISCUSSION

A. Magnetization and Curie temperature

All three experiments on $Fe_{64}Ni_{36}$ show a marked decrease in magnetization from 5 to 7 GPa, which is consistent among most studies of similar composition regardless of technique used to quantify magnetic effects under pressure [13,17–21]. That magnetization remains finite well above 7 GPa matches the results of Rueff *et al.* [19] and Nataf *et al.* [20]. Unlike previous work, we also measured magnetization during decompression; the marked increase in magnetization during the initial stages of decompression at 12.7 and 10.8 GPa appears to be a new finding. The slight increase in SIRM during compression above 13 GPa is likely significant and should be further explored to higher pressures.

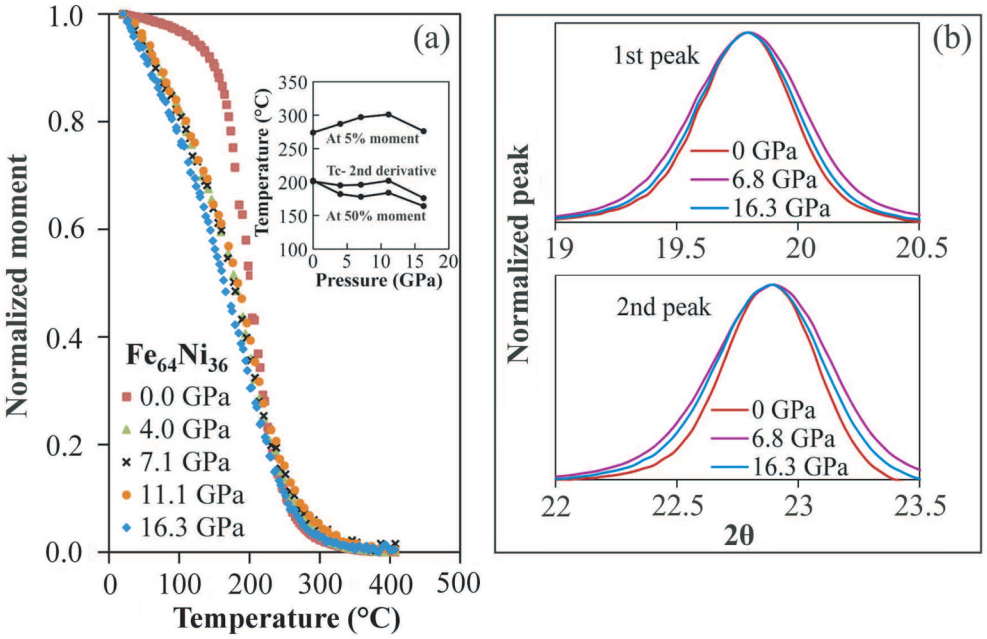

FIG. 4. (Color online) (a) Remanent magnetization normalized to the initial (25 °C) value versus temperature for $Fe_{64}Ni_{36}$ at 0 GPa (starting material) and measured after decompression from the indicated peak pressure (heating runs only). The inset shows the temperature after 50% and 95% loss in magnetization as a function of pressure as well as the Curie temperature defined by the second derivative. (b) Comparison of the first and second x-ray peaks between the noncompressed (0 GPa) sample with two that were pressure cycled to peak pressures of 6.8 and 16.3 GPa—the one to 16.3 GPa was measured after heating to 407 °C; that to 6.8 GPa was never heated.

What could cause the increase in magnetization during decompression? Using a high-energy ball mill, Gorria *et al.* [27] mechanically stressed $Fe_{64}Ni_{36}$ powder for 30 hours. They found that the strained Invar had a 150 K higher Curie temperature (650 K) than the nonstrained equivalent (500 K). From neutron diffraction spectra, they found that the lattice parameter of the strained Invar slightly increased Fe-Fe interatomic distances. We therefore postulated that the pressure cycling in our experiments likewise raised the Curie temperature, thereby accounting for our decompression data. To test this, we pressurized several subsamples of $Fe_{64}Ni_{36}$ to different peak pressures (4.0, 7.1, 11.1, and 16.3 GPa) and measured their Curie temperatures after decompression [Fig. 4(a)]. Pressure cycling broadens the spectra. Seen at 50% decay in magnetization, the Curie temperature obviously decreases with increasing pressure; whereas at 95% decay, Curie temperatures generally rise. Defining the Curie temperature using the second derivative resembles the trend at 50% decay.

A comparison of x-ray diffraction patterns between the pressure-cycled (6.8 and 16.3 GPa) and noncompressed samples reveals virtually identical peak positions yet are broader for the strained samples [Figs. 1(d) and 4(b)]. This could be due to grain-size reduction; however, if this were the case, we would expect coercivity (Bcr) to increase since reduced grain sizes should shift multidomain material toward the single domain state. Another possibility is that martensitic effects from strain accounts for the x-ray peak broadening and the smearing out of the Curie temperatures [Fig. 4(a)]. Indeed, Rietveld refinements using GSAS-II [28], carried out on noncompressed and pressure-cycled samples show no signature for grain-size reduction but clearly yield evidence for residual microstrain of 0.79% and 0.45% after decompression for the samples subjected to peak pressures of 6.8 and 16.3 GPa, respectively. Interestingly, the sample pressurized to 16.3 GPa was analyzed by x-ray diffraction after measuring its Curie temperature while the sample pressurized to 6.8 GPa was never heated. This suggests that heating to 407 °C relaxed some strain. Such an increase in residual microstrain is consistent with the volume increase associated with the martensitic transformation during compression [29]. Strain-induced martensitic effects also explain the enhanced magnetization during decompression around 10 to 13 GPa. In this way, the higher the maximum pressure, the greater the effect. Martensite production is likely linked to the degree of hydrostaticity, which varies among experiments and can potentially explain discrepancies when comparing results, including transition pressures from high to low spin states [30].

Curie temperatures change at a rate of -29 and -21 K/GPa for $Fe_{58}Ni_{42}$ and $Fe_{50}Ni_{50}$, which predicts a loss in magnetization at room temperature at ~11.0 and 23.4 GPa. For $Fe_{58}Ni_{42}$, we do observe slightly diminished SIRMs above 10 GPa compared to those below 10 GPa during compression, somewhat mimicking the curves for $Fe_{64}Ni_{36}$. We likely did not reach high enough pressures to see a measurable decrease in SIRM for $Fe_{50}Ni_{50}$. We interpret the enhanced magnetizations during decompression again to martensitic effects.

B. Magnetovolume effects on magnetic remanence

With some exception, pressure raises the remanent saturation magnetization of multidomain Fe-Ni alloys and Ni,

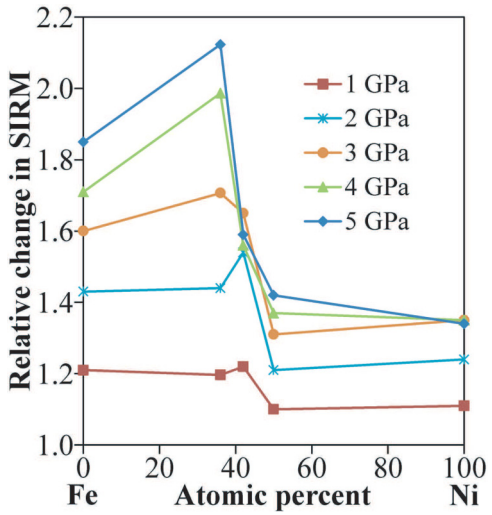

FIG. 5. (Color online) Normalized SIRM versus Ni concentration during compression to 5 GPa; pure iron data from Wei and Gilder [25].

both upon compression and especially upon decompression (Fig. 3), as it does for titanomagnetite, pyrrhotite, and pure iron [25,31,32]. A marked difference between the magnetic behavior with high pressure for Fe-Ni metals (ferromagnets) versus iron oxides or iron sulphides (ferrimagnets) is that coercivity decreases or changes little in ferromagnets, yet, with few exceptions, markedly increases in ferrimagnets.

Several sources contribute to the total magnetic energy, of which magnetic anisotropy energy (E_{anis}) will be raised by straining the lattice. $E_{\text{anis}} = (3/2)\,\lambda_s\sigma \cdot \cos^2\theta$, with λ_s being the net magnetostriction constant, σ the applied stress, and θ the angle between the magnetization vector of the grain relative to the applied stress direction [33]. From this equation one would predict that the remanent magnetizations of materials possessing higher magnetostriction coefficients will be more stress sensitive. For example, in the iron-titanium oxide solid solution series (titanomagnetite) ($Fe_{3-x}Ti_xO_4$, with x from 0 to 1), an abrupt rise in magnetostriction occurs when x exceeds 0.2 [34], which coincides with pressure-induced changes in magnetization (see Fig. 12 in Gilder and Le Goff [35]). Hence, one would also predict that the magnetization of the Invar phases that possess higher magnetostriction coefficients than other Fe-Ni alloys will be more sensitive to an imposed stress. This is indeed what we observe (Fig. 5)—an equivalent imposed stress has a greater relative effect on the magnetizations of $Fe_{58}Ni_{42}$ and $Fe_{64}Ni_{36}$ than the other alloys. Thus we attribute the increase in magnetic remanence to an increase in the magnetic anisotropy energy, which is likely augmented by strain from the martensitic transition.

IV. CONCLUSIONS

Our experiments show that pressure generally enhances the remanent magnetization intensities of Fe-Ni alloys and Ni at room temperature, whereas magnetic coercivity initially decreases then remains constant at relatively low values ($\sim$<20/mT). If the increase in remanent magnetization were due to a decrease in magnetic grain size, going from multidomain to a more single domain-like state, then one would expect coercivity to increase—opposite to what we observe. Increased magnetic interactions could decrease coercivity, but magnetic interactions would also lower the slope in magnetization approaching saturation [36], which is likewise not observed. The broadening of the x-ray diffraction patterns can be explained either by a decrease in grain size or by an increase in strain. The sum of our results clearly validates the latter, thus we conclude that the diffusionless, structural transition produced by internal shear (martensitic transformation) in the metal best accounts for the changes in magnetic remanence for all Fe-Ni metals.

Why the magnetic remanence significantly increases upon decompression in the third experiment on $Fe_{64}Ni_{36}$ is also likely due to martensitic effects. Cycling to sequentially higher pressures can test this. The implications are that the energy governing the process that enhances the magnetization largely exceeds the effect causing the decrease around 6 GPa. Gorria *et al.* [27] interpreted the suppression due to an increase in Curie temperature. Our results contradict this explanation although the stresses imposed in our experiments are more hydrostatic than in Gorria *et al.* [27]. Further experiments exploring how nonhydrostatic stresses influence the Curie temperature should bear interesting results. Future work should also ascertain the pressure when the increase in magnetic remanence ceases for fcc phases with high Ni concentrations.

ACKNOWLEDGMENTS

Editorial handling by Sarma Kancharla and an insightful anonymous review are highly appreciated. We thank the Deutsche Forschungsgemeinschaft for funding this work (project GI712/7-1) under the auspices of SPP1488. Nicolas Zander assisted with the experiments on $Fe_{64}Ni_{36}$; Geophysics Masters students from class WP5.3 in 2014 assisted with the experiments on Ni_{100}.

[1] D. L. Anderson, Science **243**, 367 (1989).
[2] W. F. Bottke, D. Nesvorny, R. E. Grimm, A. Morbidelli, and D. P. O'Brien, Nature (London) **439**, 821 (2006).
[3] A. E. Ringwood, Geochim. Cosmochim. Acta **30**, 41 (1966).
[4] J. F. Albertsen, H. P. Nielsen, and V. F. Buchwald, Phys. Scr. **27**, 314 (1983).
[5] J. I. Goldstein, E. R. D. Scott, and N. L. Chabot, Chem. Erde **69**, 293 (2009).
[6] K. B. Reuter, D. B. Williams, and J. I. Goldstein, Metall. Trans. A **20**, 719 (1989).
[7] J. Crangle and G. C. Hallam, Phys. Eng. Sci. **272**, 119 (1963).
[8] B. Glaubitz, S. Buschhorn, F. Brüssing, R. Abrudan, and H. Zabel, J. Phys.: Condens. Matter **23**, 254210 (2011).
[9] H. Asano, J. Phys. Soc. Jpn. **27**, 542 (1969).
[10] G. T. Dubovka, Phys. Status Solidi A **24**, 375 (1974).
[11] R. Bozorth and J. Walker, Phys. Rev. **89**, 624 (1953).

[12] R. J. Weiss, Proc. Phys. Soc. **82**, 281 (1963).
[13] G. Hausch, Phys. Status Solidi A **18**, 735 (1973).
[14] M. van Schilfgaarde, I. A. Abrikosov, and B. Johansson, Nature (London) **400**, 46 (1999).
[15] L. Patrick, Phys. Rev. **93**, 384 (1954).
[16] J. S. Kouvel and R. H. Wilson, J. Appl. Phys. **32**, 435 (1961).
[17] J. Leger, C. Loriers-Susse, and B. Vodar, Phys. Rev. B **6**, 4250 (1972).
[18] M. M. Abd-Elmeguid, B. Schleede, and H. Micklitz, J. Magn. Magn. Mater. **72**, 253 (1988).
[19] J. P. Rueff, A. Shukla, A. Kaprolat, M. Krisch, M. Lorenzen, F. Sette, and R. Verbeni, Phys. Rev. B **63**, 132409 (2001).
[20] L. Nataf, F. Decremps, J. Chervin, O. Mathon, S. Pascarelli, J. Kamarád, F. Baudelet, A. Congeduti, and J. P. Itié, Phys. Rev. B **80**, 134404 (2009).
[21] K. Matsumoto, H. Maruyama, N. Ishimatsu, N. Kawamura, M. Mizumaki, T. Irifune, and H. Sumiya, J. Phys. Soc. Jpn. **80**, 023709 (2011).
[22] Y. Y. Chuang, Y. A. Chang, R. Schmid, and J. C. Lin, Metall. Trans. A **17**, 1361 (1986).
[23] L. J. Swartzendruber, V. P. Itkin, and C. B. Alcock, J. Phase Equilib. **12**, 288 (1991).
[24] Q. Li, A. Wiedenmann, and H. Wollenberger, J. Mater. Res. **12**, 83 (1997).
[25] Q. Wei and S. A. Gilder, Geophys. Res. Lett. **40**, 5131 (2013).
[26] D. J. Dunlop and Ö. Özdemir, *Rock Magnetism: Fundamentals and Frontiers* (Cambridge University Press, Cambridge, 1997).
[27] P. Gorria *et al.*, Phys. Rev. B **80**, 064421 (2009).
[28] B. H. Toby and R. B. Von Dreele, J. Appl. Crystallogr. **46**, 544 (2013).
[29] E. F. Wassermann and P. Entel, J. Phys. IV **5**, C8 (1995).
[30] S. Odin, F. Baudelet, Ch. Giorgetti, E. Dartyge, J. P. Itié, A. Polian, J. C. Chervin, S. Pizzini, A. Fontaine, and J. P. Kappler, Europhys. Lett. **47**, 378 (1999).
[31] S. A. Gilder and M. Le Goff, Geophys. Res. Lett. **35**, L10302 (2008).
[32] S. A. Gilder, R. Egli, R. Hochleitner, S. C. Roud, M. W. R. Volk, M. Le Goff, and M. de Wit, J. Geophys. Res. **116**, B10101 (2011).
[33] C. Kittel, Rev. Mod. Phys. **21**, 541 (1949).
[34] Y. Syono, Jpn. J. Geophys. **4**, 71 (1965).
[35] S. A. Gilder and M. Le Goff, in *Advances in High-Pressure Technology for Geophysical Applications*, edited by J. H. Chen, Y. B. Wang, T. S. Duffy, G. Y. Shen, and L. Dobrzhinetskaya (Elsevier, New York, 2005).
[36] S. Cisowski, Phys. Earth Planet. Inter. **26**, 56 (1981).